AGU PUBLICATIONS

Geophysical Research Letters

RESEARCH LETTER
10.1002/2018GL077183

Key Points:
- Remote sensing of equatorial Bz distribution by observing the loss cone features of solar energetic electrons at low-altitude spacecraft
- Empty loss cone of 30–100 keV electrons embedded in wide isotropic precipitation regions were observed during some substorm growth phase events
- Explained as long-lived Bz-ridge-type structure at 15–20 R_E in magnetotail which are also sometimes observed in global LFM simulations

Supporting Information:
- Supporting Information S1

Correspondence to:
V. A. Sergeev,
victor@geo.phys.spbu.ru

Citation:
Sergeev, V. A., Gordeev, E. I., Merkin, V. G., & Sitnov, M. I. (2018). Does a local B-minimum appear in the tail current sheet during a substorm growth phase?. *Geophysical Research Letters*, *45*, 2566–2573. https://doi.org/10.1002/2018GL077183

Received 17 JAN 2018
Accepted 1 MAR 2018
Accepted article online 5 MAR 2018
Published online 23 MAR 2018

Does a Local B-Minimum Appear in the Tail Current Sheet During a Substorm Growth Phase?

V. A. Sergeev[1], E. I. Gordeev[1], V. G. Merkin[2], and M. I. Sitnov[2]

[1]Earth's Physics Department, Saint Petersburg State University, St. Petersburg, Russia, [2]The Johns Hopkins University Applied Physics Laboratory, Laurel, MD, USA

Abstract Magnetic configurations with $dBz/dr > 0$ in the midtail current sheet are potentially unstable to various instabilities associated with the explosive substorm onset. Their existence is hard to confirm with observations of magnetospheric spacecraft. Here we use remote sensing by low-altitude spacecraft that measured the loss cone filling rate during electron-rich solar particle event, providing information about magnetic properties of the tail current sheet. We found a latitudinally localized anisotropic 30 keV electron loss cone region embedded inside an extended region of isotropic solar electron precipitation. It was persistently observed for more than 0.5 h during isolated growth phase event by six Polar Operational Environmental Satellites spacecraft, which crossed the premidnight auroral oval. The embedded anisotropic region was observed 1° poleward of the outer radiation belt boundary over 4–5 h wide magnetic local time sector, suggesting a persistent ridge-type Bz^2/j maximum in the equatorial plasma sheet at distances 15–20 R_E. We discuss infrequent observations of such events taking into account recent results of global magnetohydrodynamic simulations.

Plain Language Summary What causes a sudden onset of substorm in the magnetotail is still a puzzle for both scientists and the public. One interesting possibility is that closed magnetic field lines in the tail current sheet may occasionally form peculiar condensations (configuration with Bz component minima and maxima somewhere in the tail), and these regions may get unstable to initiate substorms. Unfortunately, there are very little chances to identify such unstable regions by satellites flying in the magnetotail just because the tail volume is huge, whereas the spacecraft are very few. Fortunately enough, the precipitation rate of energetic electrons into the ionosphere from the tail current sheet may help us to manifest large/small Bz values in the equatorial parts of corresponding magnetic field lines remotely. We explore this opportunity and demonstrate that a few low-orbiting spacecraft passing one after another across the nightside auroral region during a substorm growth phase see the same modulation of precipitation which might indicate a presence of magnetic tube condensations at 15–20 R_E distance in the tail. Whereas a new method was successfully demonstrated, the magnetic condensation signatures are not always observed. Further investigation is required to understand the role of these phenomena for the tail stability.

1. Introduction

The average magnetotail configuration has a monotonically decreasing radial dependence of basic parameters, including plasma sheet pressure, lobe magnetic field BL, and equatorial magnetic field in the current sheet (CS) center, nominally the Bz component. Such a configuration is generally stable against interchange-/ballooning-type perturbations, and it resists earthward convection in the midtail and near-Earth plasma sheet (see Erickson & Wolf, 1980, and a review by Wolf et al., 2009). In this picture, the substorms are believed to resolve the pressure crisis by drastically changing the unfavorable configuration, by means of reconnecting the long plasma tubes and restoring intense earthward convection in the near tail region.

The stability situation may change if a region with $dBz/dr > 0$ (e.g., a local Bz minimum and maximum) appears in the magnetotail. As shown by theoretical analyses, in such a case the current sheet may become unstable against the tearing instability (Sitnov & Schindler, 2010), interchange-/ballooning-type modes (Pritchett & Coroniti, 2013), or double-gradient instability (Erkaev et al., 2007). This is considered to be the most critical property for the stability of tail-like plasma sheet configurations, in particular, for initiating the magnetic reconnection (e.g., Merkin & Sitnov, 2016). It is important to verify the existence and characteristics of such $dBz/dr > 0$ regions at distances 10–30 R_E because they are potential sites of explosive growth of basic

plasma instabilities in the magnetotail, including those which may initiate the explosive development of the substorm.

Local deviations from monotonic Bz decrease, that is, regions with $dBz/dr > 0$ and local Bz minima and maxima, have occasionally been reported, particularly, during steady convection events (Sergeev et al., 1996, Stephens et al., 2013). Such observational evidence also exists for the growth phase events. First of all, observations of magnetic fields as small as 1–2 nT at the end of the growth phase are not uncommon in the neutral sheet at distances as small as 10–12 R_E (see Ohtani & Motoba, 2017; Petrukovich et al., 2013). Taking into account a considerable magnetic flux threading the plasma sheet and the auroral oval, the occurrence of such small Bz values at $r \sim$ 10–12 R_E, may by itself suggest the formation of a Bz peak somewhere further downtail. However, the actual multispacecraft observations are not conclusive about the appearance of such Bz humps. Saito et al. (2010) analyzed the Bz profile observed by five *z*-aligned Time History of Events and Macroscale Interactions during Substorms spacecraft in a couple of events, extrapolated it (a model-dependent procedure!) into an expected radial Bn distribution and concluded that a Bz peak formed somewhere at $r >$ ~13 R_E. Petrukovich et al. (2013) specifically analyzed magnetic perturbations measured by radially separated Cluster spacecraft at 12–19 R_E distances during growth phase events. They presented four examples suggestive of negative Bz gradients (and a Bz peak somewhere), with peak Bz values up to 6–8 nT at distances ≥15 R_E (see, e.g., their Figure 7). However, in many other events no signatures of the nonmonotonic profile were seen in the same distance range, with Bz remaining to be as small as ~2 nT. Recently, Ohtani and Motoba (2017) analyzed observations of radially-separated Time History of Events and Macroscale Interactions during Substorms and Geotail spacecraft, with more strict constraints imposed to ensure sufficient accuracy of the reconstruction, and they basically confirmed the conclusions of Petrukovich et al. (2013). Therefore, even though the existence of local Bz minima/maxima seems likely in some events, systematic knowledge about $dBz/dr > 0$ regions (their occurrence, location, duration, and geometry) still remains elusive.

The equatorial Bz profile can also be inferred remotely using a low-altitude polar-orbiting spacecraft. This becomes possible if the satellite scans the latitudinal (radial, when mapped into the tail) distribution of the loss cone (LC) filling rate of energetic electrons in the plasma sheet flux tubes, which depends on magnetic field line curvature near the CS center plane. In this paper, we discuss the requirements to be met in order to apply this technique to the plasma sheet. We also present an example the growth phase event with an exceptionally good spatial and temporal coverage, to demonstrate and analyze a persistent signature manifesting the localized Bz hump in the current sheet. We also compare our observations with available global magnetohydrodynamic (MHD) simulations results and briefly discuss the hump appearance from that viewpoint.

2. Requirements of Remote Sensing Based on Energetic Electrons

As a charged particle crosses the current sheet, it undergoes a nonadiabatic pitch angle (PA) change whose amplitude depends on the ratio of magnetic field curvature radius (Rc) to the particle gyroradius (ρ). The value of this ratio depends on the equatorial magnetic field and particle characteristics, determined by the particle rigidity G = mV/e, as $Rc/\rho \approx Bz^2/(G\ dBr/dz) = Bz^2/(G\ \mu_0\ j)$. The PA scattering amplitude becomes comparable to (or exceeds) the LC width if $Rc/\rho \leq 8$ at the CS center in the standard CS models (Delcourt et al., 1996, Sergeev & Tsyganenko, 1982). This field line curvature (FLC)-related PA scattering mechanism has been confirmed in application to many important magnetospheric phenomena, including the isotropy of proton distributions throughout the plasma sheet (Wang et al., 2013), extended isotropic proton precipitation, and isotropy boundary control by the tail magnetic field (e.g., Donovan et al., 2003; Newell et al., 1998; Sergeev et al., 1993). Existence of such robust PA scattering mechanism allows us to remotely sense the equatorial Bz distribution by observing the boundaries of isotropic precipitation at low-altitude polar satellites. Following Sergeev and Kubyshkina (1996), the left panel of Figure 1 illustrates how remote sensing helps reveal the nonmonotonous equatorial Bz distributions, which are our goal in this paper. In a usual situation with Bz^2/j monotonically decreasing tailward, particles move adiabatically in the near-Earth strong dipolar magnetic field where $Rc/\rho \gg 8$. Further tailward in the CS, where $Rc/\rho < 8$, they are scattered over the LC providing isotropic precipitation at latitudes poleward of isotropy boundary (IBe). If a nonmonotonous Bz variation occurs in the tail and Bz^2/j crosses the LC scattering threshold value more than once, this results

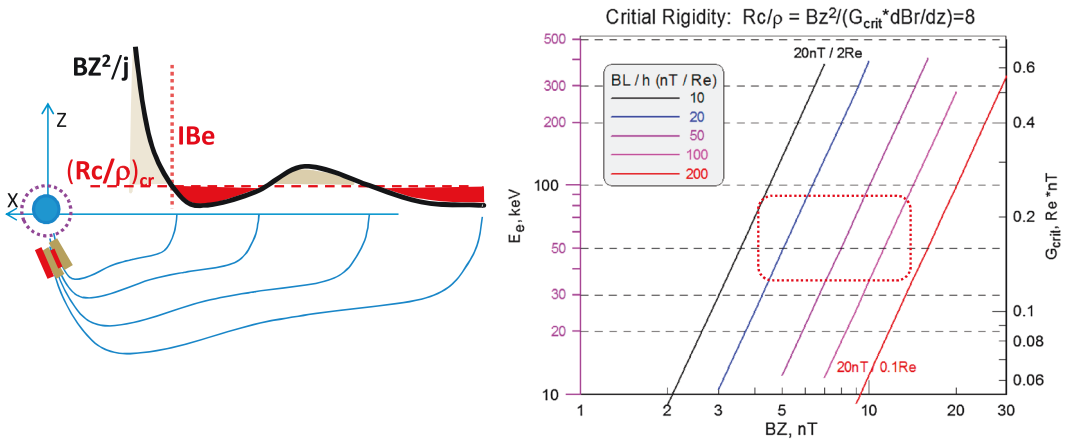

Figure 1. (left) Schematic illustrating the regions of isotropic (red shading) and anisotropic (gray shading) electron precipitation in case of nonmonotonic Bz^2/j radial variation; the threshold corresponds to the critical rigidities, for which $Rc/\rho = 8$. (right) Energy-dependent thresholds for isotropic precipitation (left axis) and the corresponding critical rigidities (right axis) as a function of equatorial Bz for different tail current densities, scaled by the lobe field BL ratio to the CS half thickness (BL/h). Also, the electron isotropy boundary (IBe) is shown in the left panel, where the loss cone precipitation sharply decreases at the low-latitude side of the current sheet.

in additional narrow region(s) of anisotropic LC precipitation (gray shading) embedded between the regions of isotropic precipitation (red shading).

The threshold Bz values for protons typically amounts several tens of nanoteslas, so they are hardly useful in the tail CS studies. For energetic electrons of 30 to 100 keV energy, computation results shown in the right panel of Figure 1 predict their Bz thresholds to be in the range from 3 to 10 nT for typical conditions at 15–20 R_E (this value can rise up to 15 nT during very thin CS conditions), making them a suitable tool to search for the tailward dBz/d*r* gradients in that region, with the Bz hump magnitude of $<\sim$10 nT (Petrukovich et al., 2013).

We use observations of polar low-orbiting Polar Operational Environmental Satellites (POES)-type satellites, each of six currently available satellites carries identical detectors to measure the energy fluxes of protons and electrons between 0.05 and 20 keV as well as more energetic particles. In particular, they measure the integral electron fluxes at $>$30, $>$100, and $>$300 keV energies near simultaneously in the LC center and outside of it (Evans & Greer, 2000). The ratio of precipitated to trapped particles (I_0/I_{90}), therefore, provides a suitable diagnostic of the LC filling rate. Previously, the examples of anisotropic LC precipitation embedded between two isotropic electron precipitation regions were demonstrated for the Steady Convection (Sergeev et al., 1996) and convection bays (Sergeev et al., 2001) conditions, in which the energetic electrons accelerated during a preceeding substorm were available as the tracers. A specific difficulty of investigating quiet periods and growth phase events is that during these times the energetic electron fluxes are typically low in the tail plasma sheet, resulting in large uncertainties in the precipitated-to-trapped flux ratio. It is also possible to use the intense flux of tracer electrons available during solar particle events. Unfortunately, events with relatively strong electron component are rare among solar particle events: by scanning through the last solar cycle 24, we found only a few events for which the count rate of $>$30 keV solar electrons in the polar cap and plasma sheet was at a level exceeding 50–100 counts per second. Investigation of a long-duration solar particle event on 15–21 May 2013 is presented here. Besides a long duration (4–5 days with high electron fluxes), this interval contained isolated activity spikes (substorms and convection events), allowing to search for the nonmonotonous Bz distributions during eight growth phase events. (Figure S1 in the supporting information shows further information about this solar particle event.)

3. Observations

The event on May 16 (event B in supporting information Figure S1) is of special interest for our study because of excellent spacecraft orbit coverage, and owing to very clear growth phase signatures of this isolated and intense substorm event. Figure 2 shows a typical pattern of precipitated energetic electrons during a solar

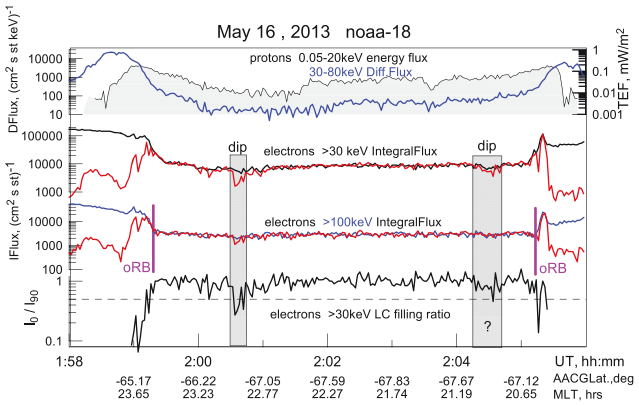

Figure 2. NOAA-18 skimming passage along the premidnight auroral zone. From top to bottom: energy flux of 0.05–20 keV protons and flux of 30–80 keV protons to characterize the plasma sheet pressure distribution; integral fluxes of $>$ 30 keV and $>$ 100 keV electrons including both precipitated (red trace) and trapped particles(black trace); ratio of precipitated to trapped fluxes of 30 keV electrons. Outer boundary of the radiation belt (labeled as oRB) is shown by purple vertical line; precipitated flux dropouts (dip) are marked by shaded rectangles. MLT = magnetic local time.

particle event, including a stable homogeneous isotropic precipitation of solar particles (plateau) at high latitudes, changing to high trapped flux (and low precipitation) in the radiation belt region at low latitudes. In this case (pass N6) the spacecraft trajectory skimmed along the oval and did not exit from the plasma sheet into the polar cap, as suggested by persistent high proton flux in the upper panel of Figure 2. The outer radiation belt boundary (oRB, defined here for 100 keV e-channel at the point where the particle flux increases sharply above its solar particle level; see Figure 2) was crossed twice, near midnight and at ~20.5 h magnetic local time (MLT). The isotropic precipitation of solar electrons was briefly interrupted at locations by ~1° of latitude poleward of the RB boundary crossings at both ends, manifested as dips of precipitated 30 keV electron flux, indicative of a partially empty LC in those regions. They are of main interest in our study as plausible signatures of the Bz humps in the equatorial magnetotail. These dip regions were not associated with noticeable changes of either precipitated proton flux (top panel of Figure 2) or the precipitated energy flux of auroral electrons (not shown here).

According to the OMNI database, in this event, under normal SW dynamic pressure of ~2 nPa, an intense (5–6 nT) southward interplanetary magnetic field (IMF) has set in started after a preceeding halfday-long quiet interval of northward IMF conditions. Following the onset of southward IMF at around 0120 UT, a distinct PC index growth indicated the convection enhancement that started at 0130 UT—Figure 3a. A sudden onset of Pi2 pulsations, midlatitude magnetic bays (not shown), and AL index at ~0235 UT indicated the end of the growth phase. The peak AE value of 670 nT qualifies this case as a strong substorm event.

During the 1 h long growth phase, six POES spacecraft passed one after another across the nightside auroral oval, as shown in Figures 3a and 3b. (The pass N5 occurred at the very beginning of the growth phase; it revealed a transitory behavior between the previous quiet time passes N1, …, N4 and the following growth phase passes N6, …, N10, which are the subject of our detailed study.) Figure 3c shows a summary of LC filling ratio profiles for five subsequent crossings N6, …, N10. In the presence of I_0/I_{90} variations (mostly because of

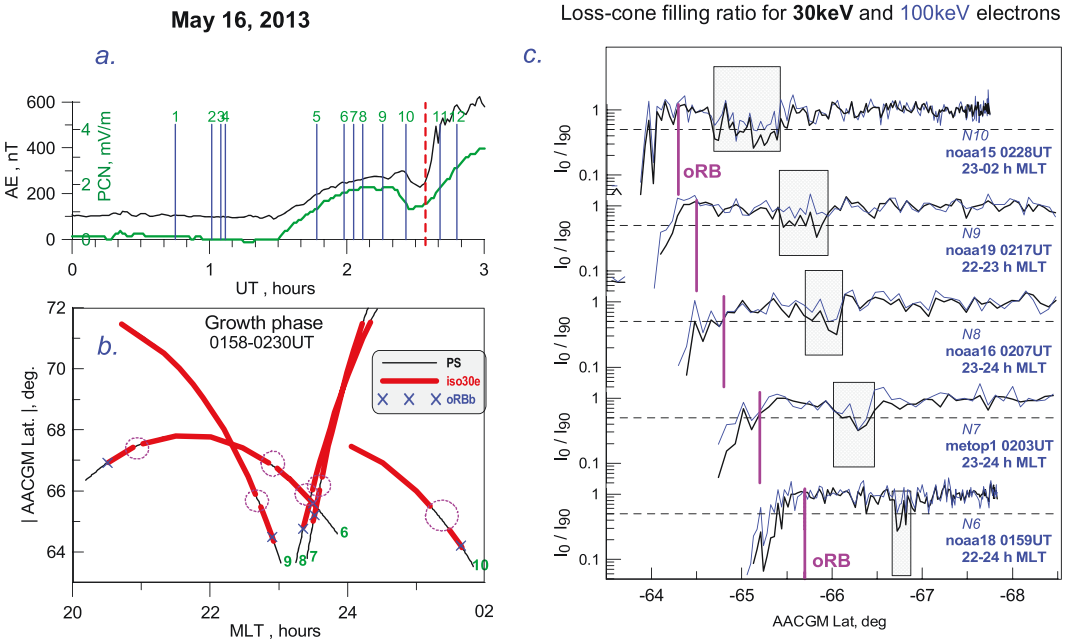

Figure 3. (a) AL and PCN indices on 16 May 2013; numbered vertical lines correspond to the nightside auroral zone crossings by POES; substorm onset is indicated by the red line. (b) POES trajectories with indication of outer RB boundaries and isotropic solar electron precipitation regions (red). (c) A summary of loss cone filling ratio changes against AACGM latitude observed in five subsequent near-midnight passes of POES spacecraft. MLT = magnetic local time.

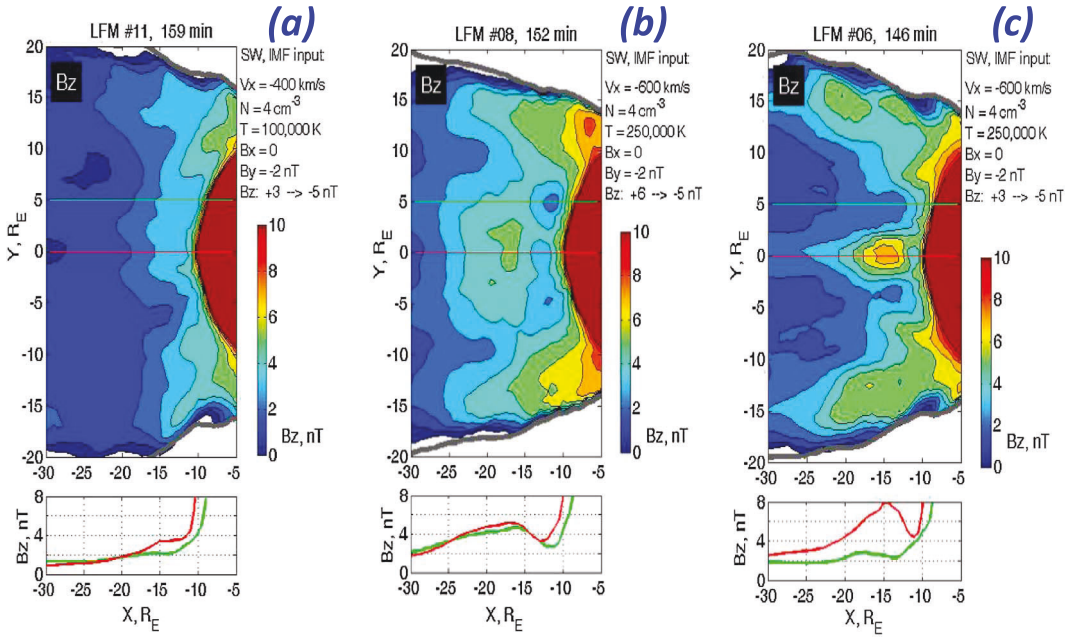

Figure 4. Results of global magnetohydrodynamic (LFM) simulations showing different types of equatorial Bz distributions in the magnetotail during late growth phase, including (a) monotonic Bz profiles, (b) azimuthally extended Bz ridge-type structure, and (c) azimuthally localized Bz hump. The solar wind input parameters are shown for each simulation at the right corner of each color panel. Bottom plots illustrate the tail-aligned equatorial Bz profiles at $Y = 0$ (red line) and at $Y = 5$ R_E (green line).

time aliasing due to alternating measurements of either precipitated or trapped fluxes in 2 s cadence) the dip regions are formally defined as those in which I_0/I_{90} falls below 0.5 for at least two subsequent measurements in the 30 keV electron channel. At $E > 100$ keV a similar dip effect can be observed simultaneously although usually it has a smaller drop amplitude (the blue curve lies above the black one in the dips), as expected for the magnetic curvature-controlled precipitation. As the time progressed, all features including the radiation belt boundary (oRB) and the dip structures shifted progressively to lower latitude, indicating the global equatorward expansion of the auroral oval (by about 1.5° in 30 min), probably corresponding to the increase of the tail current during the growth phase. The dip separation from the RB boundary stays roughly the same during this expansion, being about 1° of the altitude adjusted corrected geomagnetic latitude (AACGMLat). The dip latitudinal size varied between 0.2° and 0.7° latitude. Spatially, the oRB boundary is close to the electron isotropy boundary, IBe (where the I_0/I_{90} ratio sharply decreases at the low-latitude side close to oRB). According to estimations presented below, the IBe stays in the equatorial region at, roughly, 10 R_E distance. Consistent with this identification, the oRB also stays near the outer boundary of strong proton pressure gradient, evidenced by significant steady increase of 30 keV proton fluxes in the upper panel of Figure 2.

According to predictions of TA15 magnetospheric model (Tsyganenko & Andreeva, 2015) calculated at midnight for the 02:15 UT epoch, the critical value of Bz^2/j required for isotropic precipitation of 30 keV (and 100 keV) electrons was reached at 12 R_E (and 10.7 R_E), accordingly. The corresponding isotropy boundary field lines were mapped to 65.8° (65.6°) ACGMLat in the ionosphere, which is about 1° poleward of their actual locations in Figure 3c. The model is, therefore, understretched, and the IBe true locations are estimated to be at 9–10 R_E distance. Not a surprising fact, the Bz behaved monotonically in the model beyond the isotropy boundary, so the standard models principally cannot reproduce the local Bz hump features investigated in our study.

4. Discussion and Concluding Remarks

A distinguishing feature of nonadiabatic particle scattering in the tail current sheet is that this is a very robust and predictable mechanism, which (for a given particle mass, charge, and energy) depends only on magnetic field properties in the CS center, particularly on the Bz^2/j value. It inevitably results in an extended unstructured region of isotropically filled LC in the tail plasma sheet, as manifested by extended plateau-like

isotropic precipitation regions on closed field lines (Figures 2 and 3). No wave-particle interaction mechanism can compete with that. For 30 to 100 keV electrons the FLC mechanism predicts that the isotropic precipitation sets in as soon as Bz becomes less than, roughly, 5–10 nT for the wide range of tail current sheet parameters (see the marked area in Figure 1b). If the Bz component rises above this threshold in some region, the dip in I_0/I_{90} ratio follows as demonstrated in Figures 2 and 3c.

The next issue is the origin and geometry of the enhanced Bz region. A possibility that the spacecraft crosses the field lines connected to a BBF carrying a dipolarized magnetic field (which can occur in the plasma sheet under any activity conditions, including the growth phase, e.g., Xing et al., 2010) can be ruled out by several arguments. First, there is no change in the energy flux of auroral protons and electrons across these dips (no evidence of a pressure change or a streamer-related precipitation). The second argument is the long duration of similarly looking and positioned dip structures which are observed over more than 30 min, much longer compared to the BBF time scale ($\leq$ 10 min). The third argument is a very different geometry: rather than the azimuthally narrow channel, Figures 2 and 3 suggest instead an azimuthally extended but radially limited ridge-like geometry (see below).

The distance in the magnetosphere between the isotropy boundary of energetic electrons (or oRB) and the dip region can be estimated from the magnetic flux conservation between the ionosphere and magnetosphere in a flux tube with transverse cross-section dimensions and magnetic field intensities (ΔXi, ΔYi, Bi) and (ΔXm, ΔYm, Bm), respectively: Bi $\cdot$ ΔXi $\cdot$ ΔYi = Bm $\cdot$ ΔXm $\cdot$ ΔYm. As a rough estimate we use Bi = 58,000 nT and take into account that in the magnetotail transition region the scaling factor in *Y* direction (My = ΔYm/ΔYi) is only weakly model dependent at latitudes near the electron isotropy boundary. According to Dubyagin et al. (2002), it can be approximated as My = 27.1 + 3.12* ($|$Alat$|$ $-$ 65.8) $-$ 5.6 PSI $\cdot$ sign(Alat), where Alat is the corrected geomagnetic latitude of the electron isotropy boundary and PSI is the dipole tilt in radians. In this case, taking My ~ 30, one obtains numerically ΔXm (R_E) $\approx$ 7 (ΔXi /[1°ACGMLat]) $\cdot$ ([5 nT]/Bm), where the ionospheric distance ΔXi is expressed in degrees of latitude. If equatorial magnetic field is of the order of 5 nT, as expected in the proximity of 30 keV electron IB for the CS thickness of 1 R_E and the lobe field of 30 nT (Figure 1b), the distance in the magnetosphere between the isotropy boundary location and Bz hump is ~7 Re for the distance in the ionosphere of ~1° as observed. Therefore, the dip location is expected to be somewhere between 15 and 20 R_E in the tail. In a similar way, for the dip width of 0.2–0.7°, the scale size of the Bz hump is estimated to be from ~2 R_E to ~5 R_E depending on the actual Bz value. These anisotropic regions are observed in the near-midnight sector, at least within 22–24 h MLT (where we had four crossings), but possibly, it extends over a wider 21–01 h MLT sector (with only one crossing available on each side; see Figure 2b), which is much larger compared to the ~1 h MLT size of the typical plasma sheet BBFs. In view of dip observations spanning up to 4–5 h MLT, the dip geometry in this event corresponds to an azimuthally extended Bz ridge in the midtail.

Based on observation that the anisotropy sometimes develops simultaneously in two energy channels (30 and 100 keV) and suggesting that Rc/ρ variation was basically determined from Bz rather than from the current density variation, one may estimate the relative change of Bz amplitude in the ridge. Suggesting that Bz threshold values at 30 and 100 keV energies are scaled as square root of the corresponding electron velocities (that is $(Bz_{100}/Bz_{30})^2 \sim V_{100}/V_{30}$), this gives $Bz_{100}/Bz_{30} \geq 1.2$.

Anisotropic electron regions (dips) are not always observed. From eight growth phase events which occurred throughout the SPE on 15–19 May 2013 (see supporting information Figure S1), distinct dip events were observed during the events B, D, and F (in the latter case—only in half of the passes), whereas they were not detected in the remaining five events. One has to caution that in no event did we have coverage of POES observations in the near-midnight region as good as in the event B shown in Figures 2 and 3. Also, we should emphasize the threshold nature of the employed dip detection method, implying that Bz variation cannot be detected if both extrema (BZmin and BZmax) stay either above or below the threshold. Anyway, this limited statistics seem to indicate that the local Bz minima and regions of substantial tailward dBz/d*r* gradients may not always be observed in the real magnetotail, which is consistent with the findings of Petrukovich et al. (2013) study.

It may be important that the event B was different from other events in that it was preceded by 10 h of strong ($>$5nT) northward IMF and, hence, at that time there could be a considerable closed magnetic flux threading the plasma sheet. Because of that, the polar cap boundary was at high latitude ~71° AACGLat in the middle of

the growth phase (see passes #7–9 in Figure 3b; later on, it descended to 68° toward the substorm onset during pass 10).

To get some insight into the variable dip appearance, we looked through the results of LFM global MHD simulations recently presented by Gordeev et al. (2017), who simulated global magnetotail changes after the southward IMF turning under different solar wind inputs. Among 16 clear growth phase events, no distinct Bz minima during the growth phase were found in six events; see an example in Figure 4a for run #11. In some other runs the long-lived significant Bz minima, with max/min ratio exceeding 1.5, were found in the near tail in 10 events, including both the azimuthally extended Bz ridge cases (Figure 4b, run #8) as well as longitudinally localized structures (Figure 4c, run #6). This quick survey of the global MHD simulations showed us that, depending on the initial configuration and convection strength and distribution, different types of equatorial Bz distribution may develop. These results are consistent with our limited statistics of dip regions as well as with Petrukovich et al. (2013) analyses of Cluster observations, which suggest that the regions with substantial tailward dBz/d*r* gradient may not always be observed in the real magnetotail.

Most probably, the ridge formation can be understood as a result of fast azimuthal convective transport of closed magnetic flux from the near-Earth magnetotail to the dayside reconnection region (Hsieh & Otto, 2014). According to the global simulations presented by Gordeev et al. (2017), the magnetic flux depletion acts efficiently in a localized distance range at the periphery of the transition region (7–15 R_E) where it participates to form the local Bz minimum and tailward Bz gradient region. A more systematic study is required to further investigate this fickle and complicated Bz landscape and to reveal the generation conditions of the tailward dBz/d*r* regions in the near magnetotail.

Acknowledgments
This research was supported by the Russian Science Foundation grant 14-17-00072. We thank the data providers of POES and ACE spacecraft observations as well as of OMNI data which have been made available via CDAWeb site (http://cdaweb.gsfc.nasa.gov). LFM simulations have been performed at NASA CCMC; V. G. M. and M. I. S. would like to acknowledge support from NASA grants NNX13AF82G and NNX15AN73G. Simulation results are available at https://ccmc.gsfc.nasa.gov (runs "Evgeny_Gordeev_120314_41" through "Evgeny_Gordeev_120314_56"; the table of the run parameters is also available in Gordeev et al., 2017). V. S. thanks Nikolai Tsyganenko for his advices to improve the manuscript. This paper benefited from discussions during the meetings of ISSI team "Explosive Processes in the Magnetotail: Reconnection Onset and Associated Plasma Instabilities" led by Mikhail Sitnov. We also thank John Lyon for fruitful discussion.

References

Delcourt, D. C., Sauvaud, J.-A., Martin, R. F. Jr., & Moore, T. E. (1996). On the nonadiabatic precipitation of ions from the near-Earth plasma sheet. *Journal of Geophysical Research*, *101*(A8), 17409–17418. https://doi.org/10.1029/96JA01006

Donovan, E. F., Jackel, B. J., Voronkov, I., Sotirelis, T., Creutzberg, F., & Nicholson, N. A. (2003). Ground-based optical determination of the b2i boundary: A basis for an optical MT-index. *Journal of Geophysical Research*, *108*(A3), 1115. https://doi.org/10.1029/2001JA009198

Dubyagin, S. V., Sergeev, V. A., & Kubyshkina, M. V. (2002). On the remote sensing of plasma sheet from low altitude spacecraft. *Journal of Atmospheric and Solar - Terrestrial Physics*, *64*(5-6), 567–572. https://doi.org/10.1016/S1364-6826(02)00014-7

Erickson, G. M., & Wolf, R. A. (1980). Is steady convection possible in the Earth's magnetotail? *Geophysical Research Letters*, *7*(11), 897–900. https://doi.org/10.1029/GL007i011p00897

Erkaev, N. V., Semenov, V. S., & Biernat, H. K. (2007). Magnetic double-gradient instability and flapping waves in a current sheet. *Physical Review Letters*, *99*(23), 235003. https://doi.org/10.1103/PhysRevLett.99.235003

Evans, D. S., & Greer, M. S. (2000). Polar orbiting environmental satellite space environment monitor-2: Instrument descriptions and archive data documentation, *NOAA Tech. Memo., OAR SEC 93*, 93, version 1.4, Boulder, Colo., 2004 Jan.

Gordeev, E., Sergeev, V., Merkin, V., & Kuznetsova, M. (2017). On the origin of plasma sheet reconfiguration during the substorm growth phase. *Geophysical Research Letters*, *44*, 8696–8702. https://doi.org/10.1002/2017GL074539

Hsieh, M.-S., & Otto, A. (2014). The influence of magnetic fux depletion on the magnetotail and auroral morphology during the substorm growth phase. *Journal of Geophysical Research: Space Physics*, *119*, 3430–3443. https://doi.org/10.1002/2013JA019459

Merkin, V. G., & Sitnov, M. I. (2016). Stability of magnetotail equilibria with a tailward Bz gradient. *Journal of Geophysical Research: Space Physics*, *121*, 9411–9426. https://doi.org/10.1002/2016JA023005

Newell, P. T., Sergeev, V. A., Bikkuzina, G. R., & Wing, S. (1998). Characterizing the state of the magnetosphere: Testing the ion precipitation maxima latitude (b2i) and the ion isotropy boundary. *Journal of Geophysical Research*, *103*(A3), 4739–4745. https://doi.org/10.1029/97JA03622

Ohtani, S., & Motoba, T. (2017). Equatorial magnetic field of the near-Earth magnetotail. *Journal of Geophysical Research: Space Physics*, *122*, 8462–8478. https://doi.org/10.1002/2017JA024115

Petrukovich, A. A., Artemyev, A. V., Nakamura, R., Panov, E. V., & Baumjohann, W. (2013). Cluster observations of d*Bz*/d*x* during growth phase magnetotail stretching intervals. *Journal of Geophysical Research: Space Physics*, *118*, 5720–5730. https://doi.org/10.1002/jgra.50550

Pritchett, P. L., & Coroniti, F. V. (2013). Structure and consequences of the kinetic ballooning/interchange instability in the magnetotail. *Journal of Geophysical Research: Space Physics*, *118*, 146–159. https://doi.org/10.1029/2012JA018143

Saito, M. H., Hau, L.-N., Hung, C.-C., Lai, Y.-T., & Chou, Y.-C. (2010). Spatial profile of magnetic field in the near-Earth plasma sheet prior to dipolarization by THEMIS: Feature of minimum B. *Geophysical Research Letters*, *37*, L08106. https://doi.org/10.1029/2010GL042813

Sergeev, V. A., & Kubyshkina, M. V. (1996). Low altitude image of particle acceleration and magnetospheric reconfiguration at substorm onset. *Journal of Geomagnetism and Geoelectricity*, *48*(5), 877–885. https://doi.org/10.5636/jgg.48.877

Sergeev, V. A., Kubyshkina, M. V., Liou, K., Newell, P. T., Parks, G., Nakamura, R., & Mukai, T. (2001). Substorm and convection bay compared: Auroral and magnetotail dynamics during convection bay. *Journal of Geophysical Research*, *106*(A9), 18,843–18,855. https://doi.org/10.1029/2000JA900087

Sergeev, V. A., Malkov, M., & Mursula, K. (1993). Testing the isotropic boundary algorithm method to evaluate the magnetic field configuration in the tail. *Journal of Geophysical Research*, *98*(A5), 7609–7620. https://doi.org/10.1029/92JA02587

Sergeev, V. A., Pellinen, R. J., & Pulkkinen, T. I. (1996). Steady Magnetospheric Convection: A review of recent results. *Space Science Reviews*, *75*, 551–604.

Sergeev, V. A., & Tsyganenko, N. A. (1982). Energetic particle losses and trapping boundaries as deduced from calculations with a realistic magnetic field model. *Planetary and Space Science*, *30*(10), 999–1006. https://doi.org/10.1016/0032-0633(82)90149-0

Sitnov, M. I., & Schindler, K. (2010). Tearing stability of a multiscale magnetotail current sheet. *Geophysical Research Letters*, *37*, L08102. https://doi.org/10.1029/2010GL042961

Stephens, G. K., Sitnov, M. I., Kissinger, J., Tsyganenko, N. A., McPherron, R. L., Korth, H., & Anderson, B. J. (2013). Empirical reconstruction of storm time steady magnetospheric convection events. *Journal of Geophysical Research: Space Physics*, *118*, 6434–6456. https://doi.org/10.1002/jgra.50592

Tsyganenko, N. A., & Andreeva, V. A. (2015). A forecasting model of the magnetosphere driven by an optimal solar wind coupling function. *Journal of Geophysical Research: Space Physics*, *120*, 8401–8425. https://doi.org/10.1002/2015JA021641

Wang, C.-P., Zaharia, S. G., Lyons, L. R., & Angelopoulos, V. (2013). Spatial distributions of ion pitch angle anisotropy in the near-Earth magnetosphere and tail plasma sheet. *Journal of Geophysical Research*, *118*, 244–255. https://doi.org/10.1029/2012JA018275

Wolf, R. A., Wan, Y., Xing, X., Zhang, J.-C., & Sazykin, S. (2009). Entropy and plasma sheet transport. *Journal of Geophysical Research*, *114*, A00D05. https://doi.org/10.1029/2009JA014044

Xing, X., Lyons, L., Nishimura, Y., Angelopoulos, V., Larson, D., Carlson, C., et al. (2010). Substorm onset by new plasma intrusion: THEMIS spacecraft observations. *Journal of Geophysical Research*, *115*, A10246. https://doi.org/10.1029/2010JA015528